Semi-Transparent Perovskite Solar Cells with a Cross-Linked Hole Transport Layer

Jae Choul Yu,[1,2] Jingsong Sun,[1,2] Naresh Chandrasekaran,[1,2] Christopher J. Dunn,[3] Anthony S. R. Chesman,[3,4] and Jacek J. Jasieniak[1,2]*

[1] ARC Centre of Excellence in Exciton Science, Monash University, Clayton, Victoria 3800, Australia

[2] Department of Materials Science and Engineering, Monash University, Clayton, Victoria 3800, Australia

[3] CSIRO Manufacturing, Research Way, Clayton, Victoria 3168, Australia

[4] Melbourne Centre for Nanofabrication, Clayton, Victoria 3168, Australia

[*]Corresponding author. E-mail: jacek.jasieniak@monash.edu

Abstract

Semi-transparent perovskite solar cells (ST-PeSCs) have received great attention because of their excellent performance and promising application in areas such as tandem devices and building integrated photovoltaics (BIPVs). Critical across all these applications is achieving both high efficiency and stable photovoltaic performance of such devices. Realizing both of these properties simultaneously has not been possible using device architectures featuring the archetypal doped Spiro-OMeTAD as a hole transport layer (HTL). As such, in this work we explore the use of a solution-processed cross-linked HTL formed from N4,N4′-di(naphthalen-1-yl)-N4,N4′-bis(4-vinylphenyl)biphenyl-4,4′-diamine (VNPB) molecules as an alternative to the conventional Spiro-OMeTAD within an FTO/SnO_2/C_{60}-SAM/Perovskite/HTL/MoO_x/ultra-thin gold/MoO_x ST-PeSC device architecture. Through an optimized multi-step thermal treatment process that maximizes charge extraction and reduces recombination from these devices, we can achieve ST-PeSCs that exhibit record power conversion efficiencies for Spiro-OMeTAD-free devices with average visible transmittance values between 10 and 30%. These devices exhibit comparable efficiencies to their Spiro-OMeTAD counterparts, with the additional benefit that the use of the poly-VNPB as the HTL material provides significant improvements in long-term device stability under both continuous illumination and high humidity conditions.

Keywords: perovskite solar cells, semi-transparent, stability, hole transport layer, cross-linked layer, building integrated photovoltaics

Introduction

Solar energy is the most accessible and sustainable replacement for conventional fossil fuels. While photovoltaic devices have become commonplace in the market, a subset of this technology, semi-transparent solar cells (ST-SCs), are now receiving significant attention because they can extend the application of the technology. In particular, such devices have been earmarked for use in diverse areas, spanning high-efficiency tandem solar cells [1-6], building-integrated photovoltaics (BIPVs) [7], and vehicle-integrated photovoltaics [8]. Historically, many of these applications have been hindered by the low efficiency of available solar cell technologies that maintain semi-transparency, including those based on amorphous silicon, organics and thin-films [9]. However, this scenario has changed since the advent of metal halide perovskites. In the past decade, perovskite solar cells (PeSCs) have revolutionized the field, with continuous improvements leading to power conversion efficiencies (PCEs) of opaque architectures now exceeding 25% [10-18]. Exhibiting excellent optoelectronic properties and compatibility with low-temperature solution-based processing methods, perovskites have also emerged as promising photoabsorbers for ST-SCs [9].

Critical to achieving high performance and stability of perovskite solar cells is the appropriate selection of charge transport layers. Of these, numerous electron transport layer candidates have been identified that possess suitable stability, electronic levels and charge transport properties (e.g. TiO_2, SnO_2, PCBM). In comparison, hole transport materials (HTMs) are less developed, with 2,2′,7,7′-tetrakis(N,N-di-p-meth-oxyphenylamine)-9,9-spirobifluorene (Spiro-OMeTAD) being the most widely used HTM in conventional PeSCs (Figure 1a). However, its low hole mobility necessitates doping, typically with a bis(trifluoroethane)sulfonimide lithium salt (Li-TFSI) and 4-tert-butylpyridine (TBP), in order to yield high-performing devices. Unfortunately, Li-TFSI is highly hygroscopic [19] and TBP

can cause degradation of the perovskite film by the dissolution of PbI_2 in TBP, which limits the stability of perovskite solar cells [20].

In order to address this issue, dopant-free triphenylamine (TPA)-based compounds as HTMs in PeSCs have been reported with a PCE over 16% [21-23]. Furthermore, cross-linked polymers that offer excellent stability and mechanical durability have been suggested as alternative HTMs in perovskite solar cells [23-25]. To be compatible with a perovskite thin film, the polymer must undergo cross-linking at low temperature to avoid damaging the thermally sensitive photoactive layer. Li et al. reported the use of low-temperature cross-linkable 4,4′,4″-tris(N-carbazolyl)triphenylamine that was functionalized with two vinylbenzyl ether (TCTA-BVP) groups via a thiol-ene reaction, with the hydrophobic properties of the cross-linked TCTA-BVP significantly improving the stability of the PeSCs [23]. Meanwhile, Xu et al. demonstrated that the thermally cross-linked N4,N4-di(naphthalen-1-yl)-N4,N4′-bis(4-vinylphenyl)biphenyl-4,4′-diamine (VNPB) (Figure 1b), could similarly improve stability and efficiency in opaque PeSCs [24]. Despite the highest occupied molecular orbital (HOMO) level of the poly-VNPB being well matched to that of the perovskite layer, electrical doping by MoO_3 was found to be key to achieving sufficient conductivity to be used as an effective hole transport layer (HTL). Importantly, the poly-VNPB/MoO_3 film did not induce degradation of the perovskite active layer, which ensured that it maintained good performance, even under harsh device testing conditions. Collectively, these preliminary studies indicate that thermally cross-linked polymers create a viable pathway towards achieving stable high efficiency opaque PeSCs. Adopting these methodologies to achieve such characteristics within ST-PeSCs has to date remained unexplored.

In this work, we demonstrate the fabrication of highly efficient and stable semi-transparent perovskite solar cells that replace the conventional Spiro-OMeTAD layer with the thermally

cross-linked poly-VNPB as the HTL. Investigations show that following the initial cross-linking of VNPB on the perovskite layer with a secondary post-annealing treatment of the completed devices is necessary to enhance charge extraction and reduce the recombination of charge carriers. Using this strategy, we achieve high PCEs of between 7.4% and 16.7% at an average visible transmittance (AVT, defined here between 400–800 nm) of over 30% to 10%, respectively, which are comparable to a Spiro-OMeTAD-containing device (PCE 16.1%). Furthermore, the unencapsulated ST-PeSCs with poly-VNPB exhibit significantly enhanced stability under humid and elevated temperature conditions.

Material and methods

Materials

N,*N*-dimethylformamide (DMF, anhydrous, 99.8%), dimethyl sulfoxide (DMSO, anhydrous, 99.9%), 4-*tert*-butylpyridine (TBP, 98%), bis(trifluoromethane)sulfonimide lithium salt (Li-TFSI), C_{60}-SAM, MoO_3 cesium iodide (CsI, 99.9%), toluene, and chlorobenzene were purchased from Sigma-Aldrich. SnO_2 nanoparticle solution (15 wt.% in water), lead iodide (PbI_2, 99.9%), and lead bromide ($PbBr_2$, 99.9%) were purchased from Alfa Aesar. Spiro-OMeTAD and VNPB were purchased from Lumtec. Formamidinium iodide (FAI), methylammonium bromide (MABr) and FK209 Co-TFSI salt were purchased from Greatcell Solar. All materials were used as received without further purification.

Fabrication of semi-transparent perovskite solar cells (ST-PeSCs)

Devices were fabricated on FTO-coated glass substrates (>86% transmittance, 15Ω/sq) supplied by LATECH, which were used after being cleaned sequentially by sonicating for 10 min in DI water, acetone and IPA, drying under a stream of nitrogen gas, and then treating for 15 min under O_2-plasma (Harrick Plasma). For the fabrication of ST-PeSCs, a dilute SnO_2 (3

wt.% in DI water) nanoparticle solution (80 µl) was spin-coated at 3,000 rpm for 30s onto a cleaned FTO-coated glass substrate and annealed at 150 °C for 30 min. After annealing, the samples were transferred into a N_2-filled glovebox for further processing. C_{60}-SAM was dissolved in chlorobenzene (3 mg/mL) and spin-coated at 3,000 rpm for 30 s and annealed at 120 °C for 10 min. The perovskite precursor solution was prepared by dissolving FAI (190 mg, 1.1 mmol), PbI_2 (548.60 mg, 1.19 mmol), MABr (21.83 mg, 0.195 mmol), $PbBr_2$ (77.07 mg, 0.21 mmol), and CsI (17.67 mg, 0.068 mmol) in 1 ml DMF/DMSO (8:2 v/v). The perovskite precursor solution (80 µl) was coated onto the C_{60}-SAM layer using a two-step spin-coating process at 1,000 rpm for 10 s, followed by 6,000 rpm for 20 s [13]. During the spin-coating step at 6,000 rpm, chlorobenzene (200 µl) was deposited onto the surface after a delay of 15 s, with the substrates then annealed at 100 °C for 1 hr. The Spiro-OMeTAD solution was prepared according to a previous report [26], while the VNPB solution constituted 3 mg/mL of VNPB dissolved in toluene. The Spiro-OMeTAD or VNPB solution was spin-coated onto the perovskite layer at 3,000 rpm for 30 s. In the case of VNPB-containing devices, VNPB-coated substrates were annealed at 120 °C for 20 min and then maintained at 150 °C for 5 min to facilitate thermal crosslinking. For opaque PeSCs, an 80 nm-thick layer of gold was thermally evaporated under a baseline pressure of less than 5×10^{-6} Torr. For the ST-PeSCs comprising a DMD top electrode, MoO_x (10 nm), gold (10 nm) and MoO_x (35 nm) were deposited under similar evaporation conditions. For devices using sputtered ITO as the top electrode, an identical device architecture was used as for the DMD-based devices, except that the top Au/MoO_x layers were replaced by a single sputtered ITO layer (45 nm) (17 W, LBS500 Sputtering System). For the hole-only devices, a gold layer (80 nm) was deposited onto FTO/glass substrates by thermal evaporation to prevent the extraction of electrons from the devices. After an O_2 plasma treatment, VNPB solution was spin-coated onto the Au-coated FTO-substrates and then annealed at 120 °C for 20 min and then maintained at 150 °C for 5

min to facilitate thermal crosslinking, replicating the VNPB deposition and treatment process used in PeSC preparation. Thereafter, MoO_x (10 nm) and Au (10 nm) were successively deposited via vacuum thermal evaporation. For devices with a post-annealing thermal treatment, the complete devices were treated at an optimal temperature of 90 °C for 10 min in a N_2-filled glovebox. The masked active area of the ST-PeSCs and PeSCs was 16 mm^2.

Characterization

The PCE of the ST-PeSCs was determined through *J-V* characteristics using a VMP3 multi-channel potentiostat (BioLogic Science Instruments) under an AM 1.5G solar simulator provided by ABET technologies (Sun 3000 Class AAA). All the *J-V* characteristics of ST-PeSCs were measured in air without encapsulation. The illuminating light intensity (100 mW/cm^2) was calibrated before testing using a standard silicon reference cell. Cross-sectional and top surface SEM images were obtained using a Magellan 400 FEGSEM (FEI, USA) operated at 5 kV. The optical transmittance of ST-PeSCs were evaluated using a UV-Vis-NIR spectrophotometer (Perkin Elmer Lambda 1050) using an integrating sphere attachment. Impedance spectroscopy was performed using an impedance analyzer (Zennium, ZAHNER-electrik GmbH & Co.) over a frequency range from 0.1 Hz to 2 MHz under one-sun illumination (100 mW/cm^2). The long-term stability of ST-PeSCs was measured in a solar simulation environmental chamber (SC 340, Atlas Material Testing Tech.). The elemental composition and WF of the poly-VNPB/MoO_x was derived from X-ray photoelectron spectroscopy and ultra-violet photoelectron emission spectroscopy, respectively (Instrument Model: Nexsa, Thermo Fisher Scientific). Al Ka and He (I) source (21.21 eV) with pass energy of 200 eV (50 eV for narrow scan) and 3 eV were used to emit X-ray and UV photons, respectively. The measurements were conducted with a chamber pressure below 5.0 $\times 10^{-8}$ Torr. The work function was determined directly from the secondary cut-off

energy through the relation: Work Function = 21.21 – Secondary Cut-Off Energy. Optical constants of the layers used in the modelling of the devices were obtained by characterisation of individual material layers deposited onto silicon and onto glass using an M2000 Spectroscopic Ellipsometer (J A Woollam).

Results and discussion

The ST-PeSC devices explored in this work possessed the following device architecture: fluorine-doped tin oxide (FTO) bottom electrode, SnO_2/C_{60}-SAM electron transport layer, $Cs_{0.05}(FA_{0.85}MA_{0.15})_{0.95}Pb(I_{0.85}Br_{0.15})_3$ perovskite absorber layer, solution-processed Spiro-OMeTAD or poly-VNPB hole transport layer (HTL), and a thermally evaporated transparent dielectric-metal-dielectric (DMD) electrode (Figure 1a and b). The DMD electrode consisted of MoO_x (10 nm)/ultra-thin gold (10 nm)/MoO_x (35 nm), as used in our previous report [27]. Meanwhile, the thickness of poly-VNPB was 12 +/- 1 nm, as determined by spectroscopic ellipsometry (see Supplementary Figure S1). Cross-sectional and top surface scanning electron microscopy (SEM) measurements of our ST-PeSCs show that the poly-VNPB and DMD electrode uniformly cover the perovskite, despite their low respective thicknesses (Figure 1c and Figure S2).

In accordance with published methods, the FTO/SnO_2/C_{60}-SAM/Perovskite/poly-VNPB stacks were heated in a N_2-filled glovebox at 120 °C for 20 min and 150 °C for 5 min to induce cross-linking of the VNPB prior to electrode deposition [24]. Following the deposition of the DMD electrodes, the as-fabricated ST-PeSCs showed modest power conversion efficiencies (PCE) of less than 11%, with low short circuit currents (J_{sc}) and fill factors (*FF*) (Figure 2b, Table 1). These poor device characteristics can be attributed to charge extraction limitations caused by the poor electrical properties of poly-VNPB. It has been shown that these limitations

can be overcome within opaque perovskite devices by introducing an MoO_x interlayer between the VNPB and a thick Au electrode [24]. In that work, it was suggested that doping of poly-VNPB by MoO_x occurred simply by leaving the devices within the evaporation chamber for 10 min following the electrode deposition. We have found that this approach does not work for DMD electrodes, likely due to the lower heat generated at the poly-VNPB/MoO_x interface from the condensation of Au clusters to form the ultrathin gold layers. This hypothesis arises from the many previous studies that have shown the importance of thermal annealing in inducing doping when using MoO_x surface layers, including F8BT/MoO_x [28], NPB/MoO_x [29] and graphene/MoO_x [30]. Based on these findings, here we explored a post-annealing thermal (PAT) treatment as a facile approach to optimizing our poly-VNPB/MoO_x interfaces that harness MoO_x/Au/MoO_x DMD electrodes.

Poly-VNPB-containing ST-PeSCs fabricated using different PAT treatment times and temperatures were fabricated in order to establish the correlation between treatment conditions and device performance (see Figure 2a). As a baseline, poly-VNPB-containing ST-PeSCs were stored at RT for periods of up to 1 hour and exhibited no change in PCE. The PCE of the ST-PeSCs that were annealed at 90 °C increased with an annealing time of up to 10 min, with no further improvements observed with increased annealing times of up to 1 hr. In contrast, the ST-PeSCs annealed at 120 °C and at 150 °C showed peak efficiencies at 5 min and 1 min, respectively, which are notably lower than the PCE observed at 90 °C, and then a rapid decrease at longer annealing times. Inspection of the device characteristics indicates that at these longer times the devices exhibited increasing shunt resistances and decreasing series resistances (see Figure S3). A statistical comparison between poly-VNPB-containing ST-PeSCs processed under an optimized 10 min PAT treatment at 90 °C to those without PAT treatment, showed a

dramatically higher average PCE for the treated devices of 15.2% compared to untreated devices of only 10.5% (see Figure S5 for a more detailed comparison).

To probe the origin of these decreased ST-PeSC characteristics with PAT treatment at higher temperatures, we performed SEM measurements to check the morphology of the MoO_x (10 nm)/Au (10 nm) electrodes treated under various thermal annealing conditions (Figure S4). The electrodes annealed at 60 °C and 90 °C for 10 min showed an unchanged surface structure compared to electrodes without PAT treatment. In contrast, surface cracking and phase segregation were observed for electrodes annealed at 120 °C and 150 °C, which is clear evidence of the electrode configuration being detrimentally disrupted due to MoO_x and/or Au nucleation at these elevated temperatures [31-33].

To further investigate the photogenerated charge recombination and transfer properties of the ST-PeSCs with and without PAT treatment, impedance spectroscopy measurements were performed under illumination (Figure 2b). An equivalent circuit, which included the sheet resistance of the electrode (R_S), the charge recombination resistance (R_{rec}) and charge transfer resistance (R_{CT}) of the device, was used to fit the Nyquist plots [34-36]. R_{CT} values of 8,400 Ω/cm^2 and 29,136 Ω/cm^2 were determined for ST-PeSCs with and without PAT treatment, respectively. The smaller charge transfer resistance of the device with PAT treatment is indicative of a more efficient charge extraction process at the electrode. We ascribe this to the enhanced conductivity of the poly-VNPB film arising from MoO_x-induced doping. Meanwhile, the R_{rec} of ST-PeSCs after PAT treatment shows a higher value of 4,696 Ω/cm^2 compared to devices without PAT treatment at 1,912 Ω/cm^2. This indicates that recombination of charge carriers is favourably slower in devices with PAT treatment. Collectively, the reduced charge transfer resistance and enhanced recombination resistance of PAT-treated devices qualitatively correlate to the observed improvements in V_{oc}, J_{sc}, *FF* and, ultimately, PCE.

To understand the origin of these improvements, *J-V* curves of the hole-only devices (FTO/Au/poly-VNPB/MoO_x/Au) without and with PAT treatment were measured under dark conditions to compare the charge extraction properties of the poly-VNPB layer after PAT treatment. A sufficiently high hole conductivity of the hole transport layer is a crucial factor in achieving efficient hole extraction [35]. It was confirmed that PAT treatment gave an approximately two-fold increase in the hole conductivity of the poly-VNPB layer (Figure S6a), which evidently provided for a more efficient charge extraction at the DMD electrode.

For completeness, steady-state photoluminescence (PL) quenching experiments were also carried out. As shown in Figure S6b, the PL of the perovskites was reduced by 87% and 93% following the deposition of poly-VNPB/MoO_x without and with PAT treatment, respectively. This indicates only a slight improvement in the hole transfer process for the PAT treated poly-VNPB/MoO_x device [37, 38]; thus, suggesting that the dominant enhancement to the charge extraction is the improved conductivity of the poly-VNPB layer.

A key comparison of these optimized poly-VNPB-containing ST-PeSCs is to their conventional Spiro-OMeTAD-containing counterparts. In Figure 2c, we show the transmittance spectra of both devices using 500 nm perovskite absorber layers. Evidently, the transmittance profiles are similar, with partial light transmission being observed above ~550 nm to yield average AVT values of 10.1% and 10.2%, respectively. This expected result arises because Spiro-OMeTAD absorbs below ~550 nm, which is a spectral region dominated by the thick perovskite layers in these cells [27].

The *J-V* characteristics of the best-performing poly-VNPB-containing ST-PeSCs without and with PAT treatment, and Spiro-OMeTAD-containing devices, are shown in Figure 2d and summarized in Table 1. Notably, due to the optimized electron extraction layer, none of the devices exhibited significant variation between forward and reverse scans. Stabilized power

output measurements under maximum power point tracking (MPPT) for a PAT-treated poly-VNPB-containing ST-PeSC device provided further evidence of this fact (Figure 2e). For reference, the device integrated photocurrent density derived from external quantum efficiency (*EQE*) spectrum was 19.7 mA/cm^2 (see Figure 2f), which is in good agreement with the J_{sc} derived from the *J*-*V* measurement. The determined average PCEs of forward and back scans across these different device architectures were 10.7%, 16.7% and 16.3%, respectively. For completeness, we also fabricated opaque devices using 80 nm-thick gold with poly-VNPB. After PAT treatment, these devices also exhibited negligible hysteresis and possessed average PCE values of 19.0% (see Table S1 and Figure S7). These results show that the optimized poly-VNPB electrode configurations are as effective as Spiro-OMeTAD for achieving high-efficiency opaque and semi-transparent perovskite devices with a DMD electrode. To the best of our knowledge, the optimized PCEs obtained here are the highest values reported to date for ST-PeSCs made without Spiro-OMeTAD at an AVT of ~10%.

Given that DMDs form just one type of semi-transparent electrode configuration, here we have also fabricated ST-PeSCs with 45 nm-thick sputtered ITO as a transparent electrode. Figure S8 shows the *J*-*V* characteristics and transmittance of poly-VNPB-containing ST-PeSCs with RF-sputtered ITO (FTO/SnO_2/C_{60}-SAM/Perovskite/poly-VNPB/MoO_x/ITO). This device showed reasonable performance, with a J_{sc} of 20.85 mA/cm^2, *FF* of 61.9%, V_{oc} of 1.06 V, and a PCE of 13.7% at an AVT of 11.7%. The lower device efficiency exhibited here compared to that for the DMD electrode arises mainly due to a reduced *FF*. This can be understood based on the higher sheet resistance of the thin ITO (85 Ω/□) versus the DMD (20 Ω/□) electrodes, and could be readily overcome through the use of a thicker ITO layer to yield comparable device efficiencies. Importantly, the result indicates that the poly-VNPB/MoO_x layer is able to

prevent damage to the perovskite layer during ITO deposition by RF-sputtering, thus enabling its use as a stand-alone ST-PeSC or within a perovskite tandem device architecture.

Regardless of the electrode configuration, the PAT treatment remains the critical step to ensuring high efficiency device performance. To probe the impact of this treatment on the poly-VNPB, we have used XPS and UPS techniques to measure the Mo oxidation state and the work function (WF) of 10 nm MoO_x deposited on ITO/VNPB films. The XPS spectra of these samples both without and with PAT treatment are shown in Figure 3a. From these measurements it is evident that the deposited MoO_x is sub-stoichiometric (i.e. $x < 3$), which is characterised through the Mo^{5+} doublet being observed at the lower binding energies [39]. Secondly, the characteristic Mo 3d doublets are shifted by ~0.3 eV to higher binding energies after PAT treatment. This shift is consistent with UPS measurements shown in Figure 3b, which indicate that the WF of the MoO_x changes from ~4.87 eV to ~5.01 eV after PAT treatment. Close inspection of the valence bands further show that both samples exhibit clear signatures of MoO_x sub-gap states originating form reduced Mo 4d species with an onset of ~0.4 eV versus the WF [39, 40]. The interfacial electronic properties between organic molecules and MoO_x can be strongly governed by these sub-gap states [41]. However, given that the WF of MoO_x can itself vary between 5.3 eV and 6.8 eV [42] depending on fabrication conditions and exposure to air [43], it is difficult to decouple any changes to the WF arising from the buried interface and/or exposed surface induced by the PAT. Further insight into the electronic evolution of VNPB/MoO_x interface and the role of the Mo^{5+} sub-gap states requires more detailed studies that are outside the scope of the current work [24].

The long-term stability of ST-PeSCs is a critical factor for gauging their commercial prospects. We compared unencapsulated ST-PeSCs containing Spiro-OMeTAD and PAT-treated poly-VNPB as HTLs over 30 days under humid conditions (60% relative humidity,

25 °C), with the results shown in Figure 4a. During this time the Spiro-OMeTAD-containing ST-PeSC showed significant degradation in PCE, dropping to less than 10% of its initial PCE within 6 days. In contrast, the ST-PeSC with the poly-VNPB showed superior long-term stability, maintaining ~60% of its initial PCE. The ST-PeSCs were also measured under 360 h of continuous one-sun illumination (100 mW/cm^2) at low humidity in an environmental chamber (50 °C, 10% relative humidity). The device performance of the Spiro-OMeTAD-containing ST-PeSCs showed a 1/e PCE reduction in ~33 h. Meanwhile, the poly-VNPB-containing ST-PeSCs maintained >80% of their initial PCE after the full 360 h test (Figure 4b). These results clearly demonstrate the superior stability of poly-VNPB-containing devices stored under high humidity or continuous light illumination.

It is well known that perovskite solar cells that use Spiro-OMeTAD as an HTL suffer from heat-induced performance degradation due to the crystallization of Spiro-OMeTAD and outgassing of the TBP additive [44-47]. In contrast, the poly-VNPB has a very high thermal stability, which dramatically increases the thermal stability of ST-PeSCs. This is in agreement with previous work on its use in opaque PeSCs [24]. To determine the origin of the enhanced long-term stability of poly-VNPB-containing ST-PeSCs under humid conditions, we performed contact angle measurements on HTL-coated perovskite films (Figure 4c-f). The initial contact angle of water droplets on the perovskite/Spiro-OMeTAD and perovskite/poly-VNPB films were 72° and 88°, respectively. After a residence time of 10 min, the contact angle on the Spiro-OMeTAD film decreased significantly to 55° due to the hygroscopic nature of the Li-TFSI in the Spiro-OMeTAD film. In contrast, the contact angle of the poly-VNPB/perovskite film remained almost constant (~87°). This provides definitive evidence that the cross-linked VNPB layer serves to prevent the penetration of water into the perovskite film, which leads to an increase in the long-term stability of the device under humid conditions.

Achieving high photovoltaic performance at high AVT is an overarching technical requirement for semi-transparent building-integrated solar cell applications, such as windows. Having shown the effectiveness of the optimized poly-VNPB/DMD electrode configuration for achieving ST-PeSCs, we now turn our attention to improving the light transmittance through the device. Transfer matrix optical modelling provides a convenient approach for simulating the absorption, transmission and reflection properties of such devices prior to their fabrication [48], including an estimation of the effective current that each of the layers contributes either through loss or in the case of the perovskite generation. In Figure 5a, we show a representative breakdown of these spectrally resolved contributions for a typical ST-PeSC with a 500 nm-thick perovskite layer. Evidently, the parasitic and reflective contributions account for <15% of the total optical losses across the visible spectrum, with the perovskite layer itself responsible for the majority of the absorption. Therefore, the most facile approach towards achieving high AVT is simply through decreasing the thickness of the perovskite layer.

We prepared a series of ST-PeSCs with perovskite film thicknesses of 500, 350, 220, and 120 nm by changing the concentration of the perovskite precursor solution (1.3 M, 1.0 M, 0.7 M, and 0.4 M, respectively). The transmittance spectra of the completed devices using these perovskite layers are shown in Figure 5b. As expected, a clear increase in transmittance was observed as the perovskite layer thickness was reduced. To understand the impact of this on the overall transmitted color of the device, we converted the measured transmittance spectra to color coordinates and located them on the CIE 1931 color chromaticity diagram (see Figure 5c). Evidently, the devices are brown in color at thicker perovskite thicknesses, then progressively change to orange, yellow and then towards color-neutrality as the thickness is reduced. These variations in transmittance and color chromaticity have been adequately modelled using the transfer matrix approach (see Figure S9) [48]. The good agreement between

predicted and measured transmittance spectra and color coordinates provides a high-level validation for the suitability of such simple optical models to describe ST-PeSCs.

The photovoltaic performance of the ST-PeSCs with various thicknesses of perovskite film is shown in Figure 5d and summarized in Table S2. The results show that devices with AVTs ranging from 10.1% to 29.5% result in PCEs of 16.1% to 7.4%, respectively. A large component of this reduced efficiency for the higher AVT devices arises from the decreased J_{sc} owing to lower total light absorption. This is confirmed through the good agreement between the observed and predicted J_{sc} derived from the above-mentioned transfer matrix modelling (see Figure 5e). Assuming that the device V_{oc} and *FF* are equivalent to that of the 500 nm-thick perovskite sample, i.e. 1.06 V and 0.744, respectively, this simulated *Jsc* can be converted to a predicted PCE as a function of perovskite thickness (see Figure 5f). This trend is in good agreement at perovskite thicknesses of 220 nm and above, while for 120 nm-thick perovskite layers it shows a major deviation. The efficiency reduction arises from a comparative decrease in V_{oc} and *FF* at such low thicknesses, which suggests a variation in the underlying device physics. Previous work has indeed indicated that such reductions may arise from interfacial and film inhomogeneities at low perovskite thickness [49]. This is likely due to the rough nature of the glass/FTO substrates that are employed in our devices.

Finally, in Figure 5f we show the PCE as a function of AVT for our poly-VNPB-containing ST-PeSCs and state-of-the-art Spiro-OMeTAD-free ST-PeSCs. This comparison has been made with inverted and normal type devices (doped PTAA-containing ST-PeSCs) [49-54],[55, 56]. The VNPB-containing devices exhibit record PCEs across most AVT values reported for Spiro-OMeTAD-free ST-PeSCs in the literature to date, with the only exception being the ultra-high AVT device reported by the group of Brabec for an inverted ST-PeSC device architecture [49]. This is clear evidence that optimized VNPB/MoO_x interfaces provide a stable

and high-efficiency charge transport layer configuration for ST-PeSCs. Nonetheless, a comparison of these results to the predicted theoretical efficiencies based on a 90% Shockley-Queisser (S-Q) limit (V_{oc}: 1.25 V [57], *FF*: 90% [58]), clearly shows that further efficiency enhancements to between 23% at an AVT of 10% and 9% at an AVT of 45% should be achievable through further material and device engineering advances that act to increase V_{oc} and FF.

Conclusions

In summary, we have successfully demonstrated highly stable semi-transparent perovskite solar cells (ST-PeSCs) by introducing the thermally cross-linked polymer formed by the polymerisation of VNPB as an alternative hole transport layer (HTL) to Spiro-OMeTAD. It was found that to achieve high efficiency, post annealing of the completed devices featuring the poly-VNPB and an MoO_x/Au/MoO_x dielectric-metal-dielectric transparent electrode was essential. In this process, the overall photovoltaic performance of the ST-PeSCs was improved from 10.7% to 16.7% at an average visible transmittance of ~10%. This improvement was attributed to enhanced charge extraction and suppressed recombination of photo-generated charge carriers in the devices, which likely arise from the improved conductivity of poly-VNPB following doping by the MoO_x. These optimized poly-VNPB-containing devices exhibited comparable efficiencies to those made using Spiro-OMeTAD, while offering dramatically improved stability under both continuous illumination and high-humidity conditions. Furthermore, ST-PeSCs made using different thicknesses of the perovskite absorber yielded color-tunable devices with record efficiencies across most measured AVT values. These findings show that the use of thermally cross-linked polymers within ST-PeSC devices provides a facile approach towards improving their performance and long-term stability, which are critical factors towards progressing such devices towards commercialization.

Appendix A. Supporting materials

Supporting data associated with this article can be found in the online version at

Acknowledgements

This activity received funding from ARENA as part of ARENA's Research and Development Program – Solar PV Research under the grant JJ007, as well as the Australian Research Council under the grant CE170100026. The authors acknowledge use of facilities within the Monash X-ray Platform. This work was performed in part at the Melbourne Centre for Nanofabrication (MCN) in the Victorian Node of the Australian National Fabrication Facility (ANFF).

References

[1] C.U. Kim, J.C. Yu, E.D. Jung, I.Y. Choi, W. Park, H. Lee, I. Kim, D.-K. Lee, K.K. Hong, M.H. Song, K.J. Choi, Nano Energy, 60 (2019) 213-221.

[2] L. Mazzarella, Y.-H. Lin, S. Kirner, A.B. Morales-Vilches, L. Korte, S. Albrecht, E. Crossland, B. Stannowski, C. Case, H.J. Snaith, R. Schlatmann, Advanced Energy Materials, 9 (2019) 1803241.

[3] F. Sahli, J. Werner, B.A. Kamino, M. Bräuninger, R. Monnard, B. Paviet-Salomon, L. Barraud, L. Ding, J.J. Diaz Leon, D. Sacchetto, G. Cattaneo, M. Despeisse, M. Boccard, S. Nicolay, Q. Jeangros, B. Niesen, C. Ballif, Nature Materials, 17 (2018) 820-826.

[4] D. Zhao, C. Chen, C. Wang, M.M. Junda, Z. Song, C.R. Grice, Y. Yu, C. Li, B. Subedi, N.J. Podraza, X. Zhao, G. Fang, R.-G. Xiong, K. Zhu, Y. Yan, Nature Energy, 3 (2018) 1093-1100.

[5] H. Shen, T. Duong, J. Peng, D. Jacobs, N. Wu, J. Gong, Y. Wu, S.K. Karuturi, X. Fu, K. Weber, X. Xiao, T.P. White, K. Catchpole, Energy & Environmental Science, 11 (2018) 394-406.

[6] J. Zheng, C.F.J. Lau, H. Mehrvarz, F.-J. Ma, Y. Jiang, X. Deng, A. Soeriyadi, J. Kim, M. Zhang, L. Hu, X. Cui, D.S. Lee, J. Bing, Y. Cho, C. Chen, M.A. Green, S. Huang, A.W.Y. Ho-Baillie, Energy & Environmental Science, 11 (2018) 2432-2443.

[7] P. Heinstein, C. Ballif, L.-E. Perret-Aebi, InGreen (2013) 125.

[8] A.A.F. Husain, W.Z.W. Hasan, S. Shafie, M.N. Hamidon, S.S. Pandey, Renewable and Sustainable Energy Reviews, 94 (2018) 779-791.

[9] J. Sun, J.J. Jasieniak, Journal of Physics D: Applied Physics, 50 (2017) 093001.

[10] A. Kojima, K. Teshima, Y. Shirai, T. Miyasaka, Journal of the American Chemical Society, 131 (2009) 6050-6051.

[11] E.H. Jung, N.J. Jeon, E.Y. Park, C.S. Moon, T.J. Shin, T.-Y. Yang, J.H. Noh, J. Seo, Nature,

567 (2019) 511-515.

[12] Q. Jiang, Y. Zhao, X. Zhang, X. Yang, Y. Chen, Z. Chu, Q. Ye, X. Li, Z. Yin, J. You, Nature Photonics, 13 (2019) 460-466.

[13] J.C. Yu, S. Badgujar, E.D. Jung, V.K. Singh, D.W. Kim, J. Gierschner, E. Lee, Y.S. Kim, S. Cho, M.S. Kwon, M.H. Song, Advanced Materials, 31 (2019) 1805554.

[14] D.-Y. Son, S.-G. Kim, J.-Y. Seo, S.-H. Lee, H. Shin, D. Lee, N.-G. Park, Journal of the American Chemical Society, 140 (2018) 1358-1364.

[15] Best Research-Cell Efficiencies (NREL, 2019) http://www.nrel.gov/pv/assets/images/efficiency-chart.png.2019.

[16] F. Zhang, W. Shi, J. Luo, N. Pellet, C. Yi, X. Li, X. Zhao, T.J.S. Dennis, X. Li, S. Wang, Y. Xiao, S.M. Zakeeruddin, D. Bi, M. Grätzel, Advanced Materials, 29 (2017) 1606806.

[17] F. Zhang, D. Bi, N. Pellet, C. Xiao, Z. Li, J.J. Berry, S.M. Zakeeruddin, K. Zhu, M. Grätzel, Energy & Environmental Science, 11 (2018) 3480-3490.

[18] F. Zhang, C. Xiao, X. Chen, B.W. Larson, S.P. Harvey, J.J. Berry, K. Zhu, Joule, 3 (2019) 1452-1463.

[19] Z. Hawash, L.K. Ono, Y. Qi, Advanced Materials Interfaces, 5 (2018) 1700623.

[20] W. Li, H. Dong, L. Wang, N. Li, X. Guo, J. Li, Y. Qiu, Journal of Materials Chemistry A, 2 (2014) 13587-13592.

[21] X. Zhao, F. Zhang, C. Yi, D. Bi, X. Bi, P. Wei, J. Luo, X. Liu, S. Wang, X. Li, S.M. Zakeeruddin, M. Grätzel, Journal of Materials Chemistry A, 4 (2016) 16330-16334.

[22] F. Zhang, X. Liu, C. Yi, D. Bi, J. Luo, S. Wang, X. Li, Y. Xiao, S.M. Zakeeruddin, M. Grätzel, ChemSusChem, 9 (2016) 2578-2585.

[23] F. Zhang, C. Yi, P. Wei, X. Bi, J. Luo, G. Jacopin, S. Wang, X. Li, Y. Xiao, S.M. Zakeeruddin, M. Grätzel, Advanced Energy Materials, 6 (2016) 1600401.

[24] J. Xu, O. Voznyy, R. Comin, X. Gong, G. Walters, M. Liu, P. Kanjanaboos, X. Lan, E.H.

Sargent, Advanced Materials, 28 (2016) 2807-2815.

[25] Z. Zhu, D. Zhao, C.-C. Chueh, X. Shi, Z. Li, A.K.Y. Jen, Joule, 2 (2018) 168-183.

[26] J.C. Yu, D.B. Kim, G. Baek, B.R. Lee, E.D. Jung, S. Lee, J.H. Chu, D. Lee, K.J. Choi, S. Cho, M.H. Song, Adv. Mater., 27 (2015) 3492.

[27] E. Della Gaspera, Y. Peng, Q. Hou, L. Spiccia, U. Bach, J.J. Jasieniak, Y.-B. Cheng, Nano Energy, 13 (2015) 249-257.

[28] M.C. Gwinner, R.D. Pietro, Y. Vaynzof, K.J. Greenberg, P.K.H. Ho, R.H. Friend, H. Sirringhaus, Advanced Functional Materials, 21 (2011) 1432-1441.

[29] P.-C. Kao, Z.-H. Chen, H.-E. Yen, T.-H. Liu, C.-L. Huang, Japanese Journal of Applied Physics, 57 (2018) 03DA04.

[30] A.N. Mehta, W. Mu, M. Murugesan, Y. Jiao, Y. Fu, P. Hyldgaard, J. Liu, Journal of Materials Science: Materials in Electronics, 29 (2018) 5239-5252.

[31] Y.J. Lee, C.W. Park, D.G. Kim, W.T. Nichols, S.T. Oh, Y.D. Kim, Journal of Ceramic Processing Research, 11 (2010) 52-55.

[32] T.S. Sian, G.B. Reddy, Solar Energy Materials and Solar Cells, 82 (2004) 375-386.

[33] V.L. De Los Santos, D. Lee, J. Seo, F.L. Leon, D.A. Bustamante, S. Suzuki, Y. Majima, T. Mitrelias, A. Ionescu, C.H.W. Barnes, Surface Science, 603 (2009) 2978-2985.

[34] M. Li, X. Yan, Z. Kang, Y. Huan, Y. Li, R. Zhang, Y. Zhang, ACS Applied Materials & Interfaces, 10 (2018) 18787-18795.

[35] J.C. Yu, J.A. Hong, E.D. Jung, D.B. Kim, S.-M. Baek, S. Lee, S. Cho, S.S. Park, K.J. Choi, M.H. Song, Scientific Reports, 8 (2018) 1070.

[36] J. Liu, C. Gao, X. He, Q. Ye, L. Ouyang, D. Zhuang, C. Liao, J. Mei, W. Lau, ACS Applied Materials & Interfaces, 7 (2015) 24008-24015.

[37] F. Zhang, Z. Wang, H. Zhu, N. Pellet, J. Luo, C. Yi, X. Liu, H. Liu, S. Wang, X. Li, Y. Xiao, S.M. Zakeeruddin, D. Bi, M. Grätzel, Nano Energy, 41 (2017) 469-475.

[38] F. Zhang, S. Wang, H. Zhu, X. Liu, H. Liu, X. Li, Y. Xiao, S.M. Zakeeruddin, M. Grätzel, ACS Energy Letters, 3 (2018) 1145-1152.

[39] J.J. Jasieniak, J. Seifter, J. Jo, T. Mates, A.J. Heeger, Advanced Functional Materials, 22 (2012) 2594-2605.

[40] M. Kröger, S. Hamwi, J. Meyer, T. Riedl, W. Kowalsky, A. Kahn, Applied Physics Letters, 95 (2009) 123301.

[41] Streetman, B. G., Banerjee, S., Solid State electronic devices, 5th ed. Prentice Hall, Upper Saddle River, N.J, 2000.

[42] Irfan, H. Ding, Y. Gao, C. Small, D.Y. Kim, J. Subbiah, F. So, Applied Physics Letters, 96 (2010) 243307.

[43] J. Meyer, R. Khalandovsky, P. Görrn, A. Kahn, Advanced Materials, 23 (2011) 70-73.

[44] N. Rolston, B.L. Watson, C.D. Bailie, M.D. McGehee, J.P. Bastos, R. Gehlhaar, J.-E. Kim, D. Vak, A.T. Mallajosyula, G. Gupta, A.D. Mohite, R.H. Dauskardt, Extreme Mechanics Letters, 9 (2016) 353-358.

[45] T. Malinauskas, D. Tomkute-Luksiene, R. Sens, M. Daskeviciene, R. Send, H. Wonneberger, V. Jankauskas, I. Bruder, V. Getautis, ACS Applied Materials & Interfaces, 7 (2015) 11107-11116.

[46] C.D. Bailie, E.L. Unger, S.M. Zakeeruddin, M. Grätzel, M.D. McGehee, Physical Chemistry Chemical Physics, 16 (2014) 4864-4870.

[47] A. Abate, T. Leijtens, S. Pathak, J. Teuscher, R. Avolio, M.E. Errico, J. Kirkpatrik, J.M. Ball, P. Docampo, I. McPherson, H.J. Snaith, Physical Chemistry Chemical Physics, 15 (2013) 2572-2579.

[48] G.F. Burkhard, E.T. Hoke, M.D. McGehee, Advanced Materials, 22 (2010) 3293-3297.

[49] C.O. Ramírez Quiroz, I. Levchuk, C. Bronnbauer, M. Salvador, K. Forberich, T. Heumüller, Y. Hou, P. Schweizer, E. Spiecker, C.J. Brabec, Journal of Materials Chemistry A,

3 (2015) 24071-24081.

[50] C. Roldán-Carmona, O. Malinkiewicz, R. Betancur, G. Longo, C. Momblona, F. Jaramillo, L. Camacho, H.J. Bolink, Energy & Environmental Science, 7 (2014) 2968-2973.

[51] S. Bag, M.F. Durstock, Nano Energy, 30 (2016) 542-548.

[52] G.M. Kim, T. Tatsuma, Scientific Reports, 7 (2017) 10699.

[53] F. Guo, H. Azimi, Y. Hou, T. Przybilla, M. Hu, C. Bronnbauer, S. Langner, E. Spiecker, K. Forberich, C.J. Brabec, Nanoscale, 7 (2015) 1642-1649.

[54] C.-Y. Chang, Y.-C. Chang, W.-K. Huang, K.-T. Lee, A.-C. Cho, C.-C. Hsu, Chemistry of Materials, 27 (2015) 7119-7127.

[55] J.H. Heo, M.H. Jang, M.H. Lee, H.J. Han, M.G. Kang, M.L. Lee, S.H. Im, Journal of Materials Chemistry A, 4 (2016) 16324-16329.

[56] J.H. Heo, J. Han, D.H. Shin, S.H. Im, Materials Today Energy, 5 (2017) 280-286.

[57] S. Gharibzadeh, B. Abdollahi Nejand, M. Jakoby, T. Abzieher, D. Hauschild, S. Moghadamzadeh, J.A. Schwenzer, P. Brenner, R. Schmager, A.A. Haghighirad, L. Weinhardt, U. Lemmer, B.S. Richards, I.A. Howard, U.W. Paetzold, Advanced Energy Materials, 9 (2019) 1803699.

[58] M. Stolterfoht, C.M. Wolff, Y. Amir, A. Paulke, L. Perdigón-Toro, P. Caprioglio, D. Neher, Energy & Environmental Science, 10 (2017) 1530-1539.

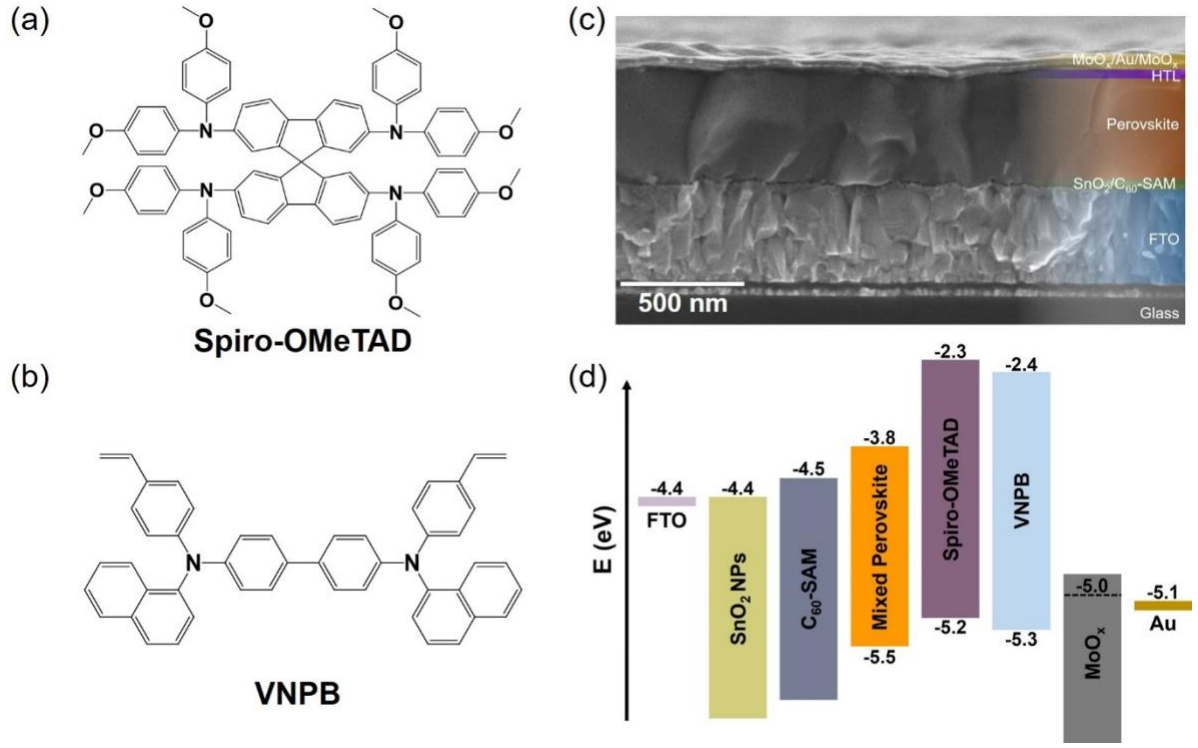

Figure 1. The chemical structure of (a) Spiro-OMeTAD and (b) VNPB. (c) Cross-sectional scanning electron microscopy (SEM) image of a semi-transparent perovskite solar cell (ST-PeSC) and (d) relative energy levels of the device components in the ST-PeSCs.

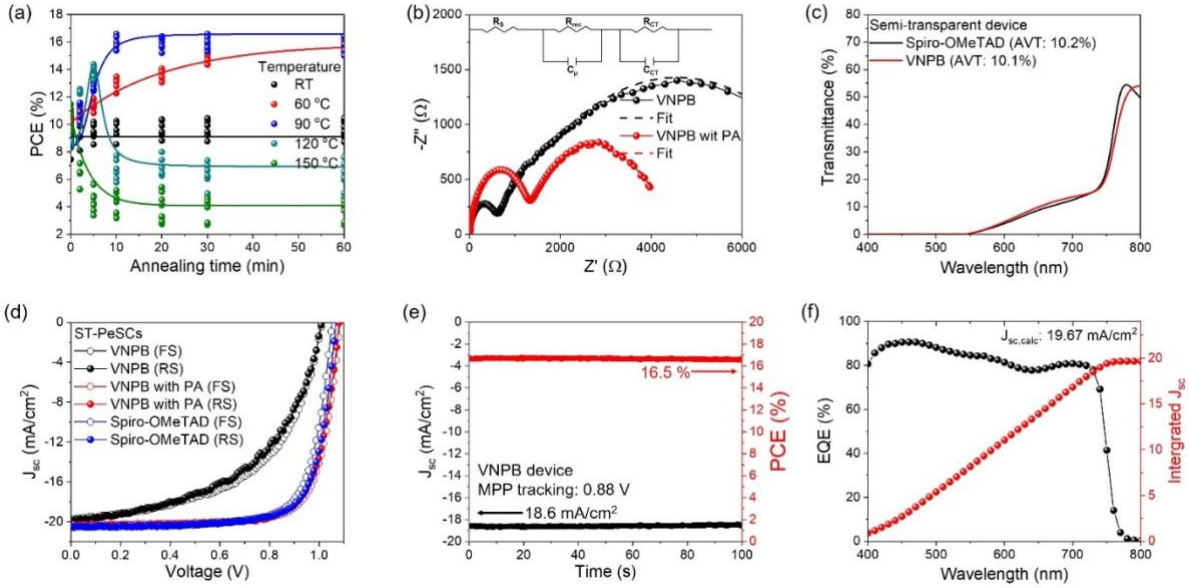

Figure 2. (a) Changes in PCE for PAT-treated VNPB-containing ST-PeSCs with respect to different annealing temperatures and time. The lines are showing a logistic fit to the experiment data points. (b) Nyquist plots of VNPB-containing ST-PeSCs without and with PAT treatment. The inset figure shows the equivalent circuit model for ST-PeSCs. (c) Transmittance spectra of whole Spiro-OMeTAD- and VNPB-containing ST-PeSCs. (d) Comparison of *J*-*V* curves of Spiro-OMeTAD- and VNPB-containing ST-PeSCs without and with PAT treatment. (e) Steady-state power conversion efficiencies of VNPB-containing ST-PeSCs monitored at the V_{mpp} of 0.88 V for 100 s. (f) External quantum efficiency (*EQE*) and integrated photocurrent density of VNPB-based ST-PeSCs.

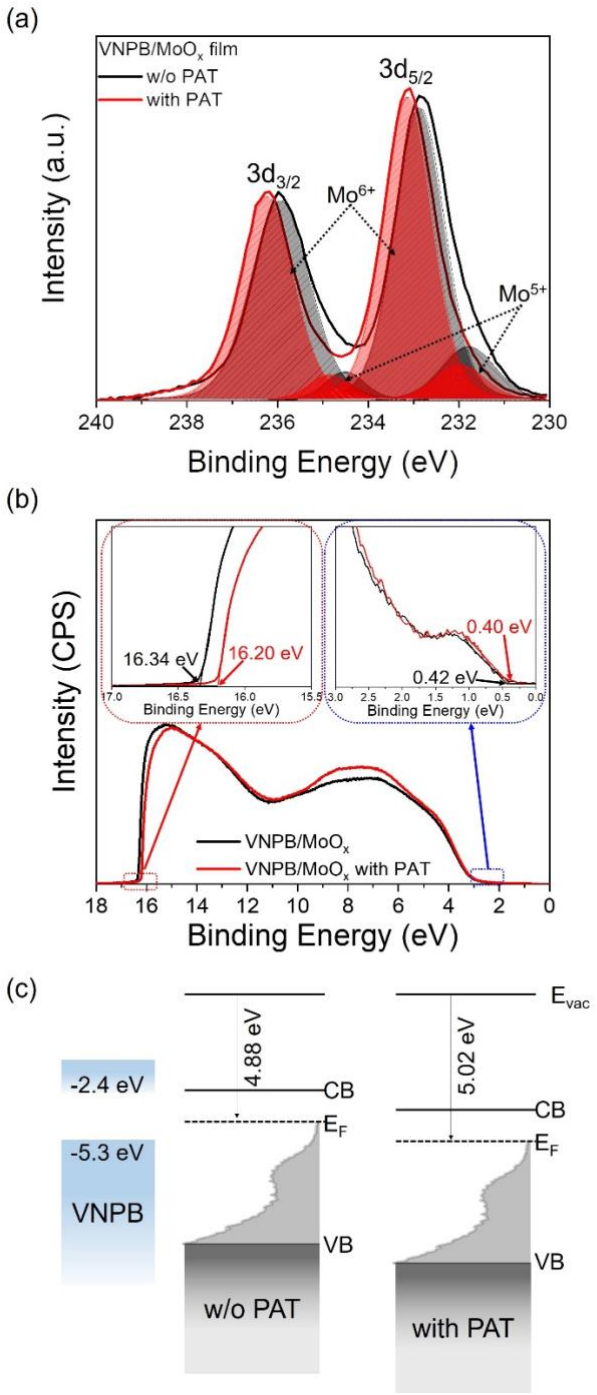

Figure 3. XPS surveys of a 10 nm MoO_x film on a VNPB film on an ITO-coated substrate without and with PAT treatment, Mo 3d core level. The Mo 3d spectra of MoO_x on a VNPB film without and with PAT treatment, modelled using CasaXPS software. (b) UPS spectra of MoO_x on a VNPB film without and with PAT treatment (inset figure showing detailed spectra of secondary electron cut-off (red arrow) and the sub-bandgap state (blue arrow) region, respectively). (c) Energy level diagram with respect to vacuum level for the VNPB/MoO_x film without and with PAT treatment.

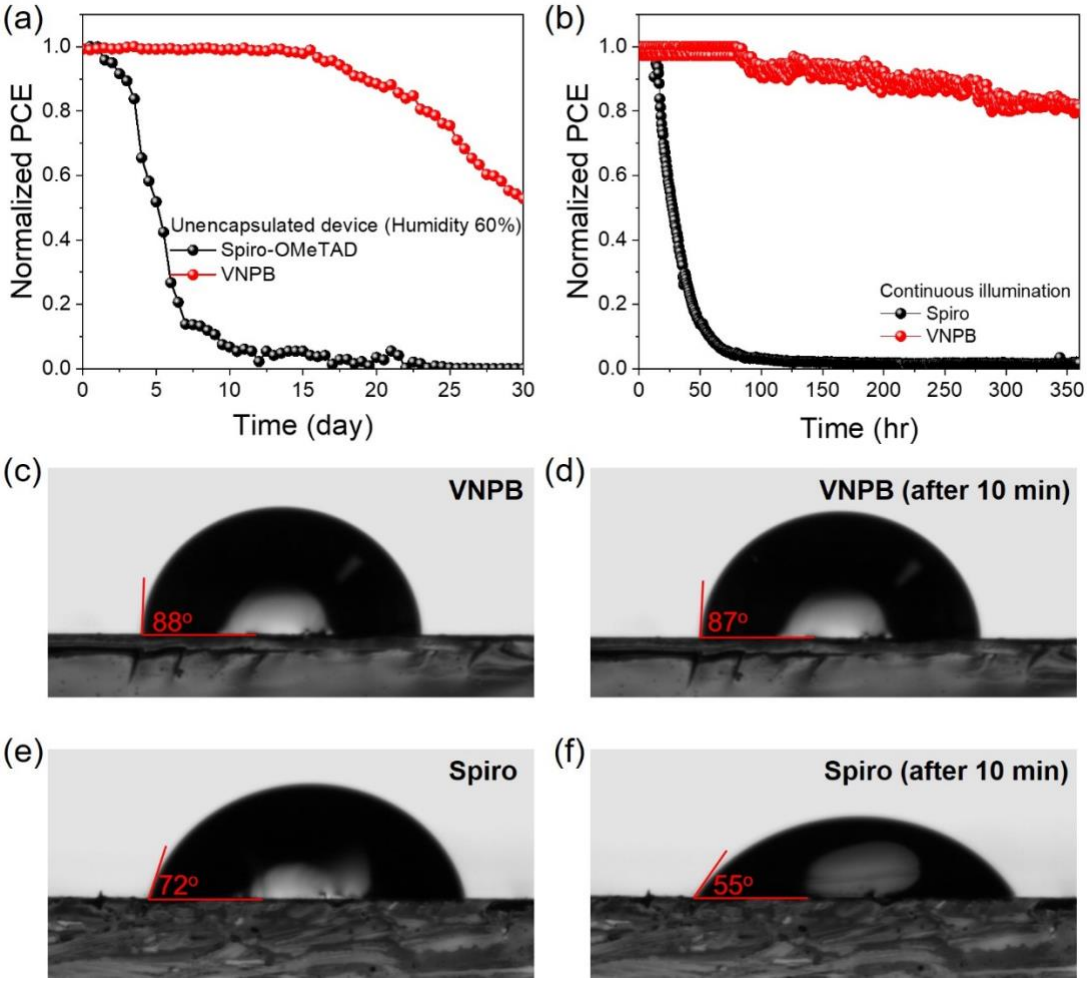

Figure 4. Stability characteristics of unencapsulated ST-PeSCs with Spiro-OMeTAD or VNPB as an HTL under (a) non-continuous one-sun AM 1.5G (100 mW/cm^2) illumination (25 °C, 60% humidity) and (b) continuous one-sun illumination (50 °C, 10% humidity). (c-f) Contact angles of a water droplet on VNPB or Spiro-OMeTAD on perovskite films.

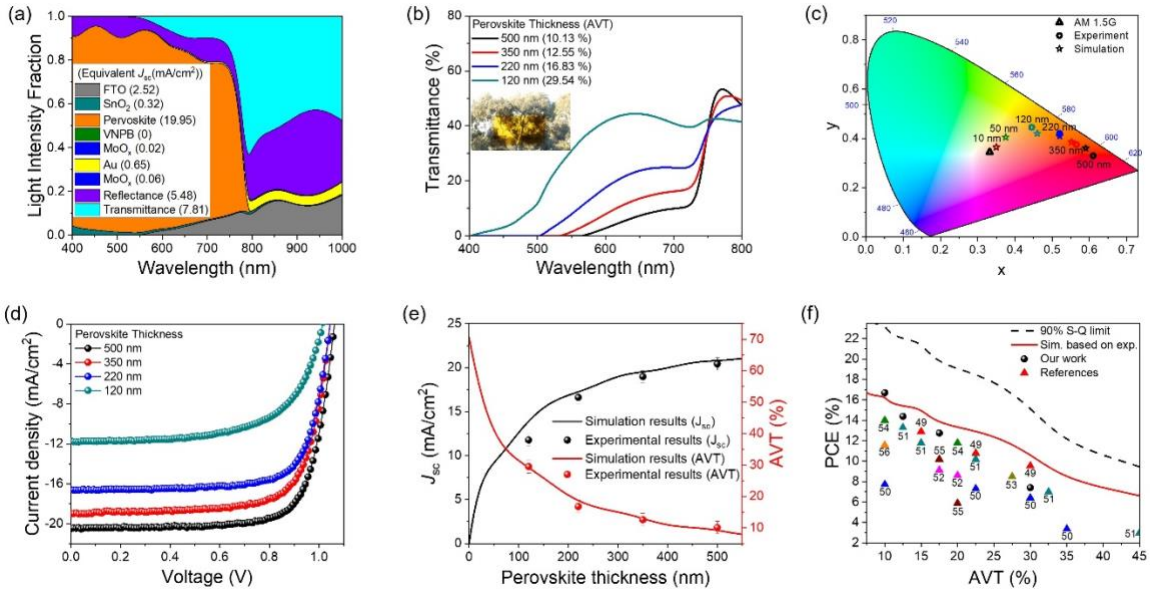

Figure 5. (a) Optical simulation results based on the transfer matrix optical model for ST-PeSCs and the equivalent current density from each layer is shown on each layer. (b) Experimental transmittance spectra of whole VNPB-containing ST-PeSCs with different perovskite film thicknesses. The inset shows a photograph of a ST-PeSC with 120 nm perovskite thickness. (c) Color coordinates on the CIE 1931 chromaticity diagram of ST-PeSCs with perovskite films of different thicknesses. (d) *J-V* characteristics of VNPB-containing ST-PeSCs with perovskite films of different thicknesses. (e) The perovskite film thickness dependence of current density and AVT of VNPB-containing ST-PeSCs: dash curve, simulation results based on 90% Shockley-Queisser (S-Q) limit (V_{oc}: 1.25 V, *FF*: 90%), full curve, simulation results based on experimental results (V_{oc}: 1.05 V, *FF*: 75%), full spheres, experimental results. (f) Plot of PCE as a function of AVT and comparison with other Spiro-OMeTAD-free ST-PeSCs (inverted type device[49-54] and doped PTAA-containing device[55, 56]).

Table 1. Summary of device performance of Spiro-OMeTAD-containing ST-PeSCs and VNPB-containing ST-PeSCs without and with PAT treatment.

Device configuration	J_{SC} [mA/cm]	V_{oc} [V]	FF	η [%]
FTO/ETL/Perovskite/VNPB/DMD (FS)	19.746	1.013	0.546	10.91
FTO/ETL/Perovskite/VNPB/DMD (RS)	19.865	1.010	0.521	10.46
FTO/ETL/Perovskite/VNPB/DMD, PAT treated (FS)	20.352	1.084	0.758	16.72
FTO/ETL/Perovskite/VNPB/DMD, PAT treated (RS)	20.436	1.081	0.743	16.41
FTO/ETL/perovskite/Spiro-OMeTAD/DMD (FS)	20.522	1.052	0.745	16.07
FTO/ETL/perovskite/Spiro-OMeTAD/DMD (RS)	20.482	1.068	0.753	16.45

The table of contents entry

Keyword: perovskite solar cells, semi-transparent, stability, hole transport layer, cross-linked layer, building integrated photovoltaics

Jae Choul Yu,[1,2] Jingsong Sun,[1,2] Naresh Chandrasekaran,[1,2] Christopher J. Dunn, [3]

Anthony S. R. Chesman,[3,4] and Jacek J. Jasieniak[1,2]*

Semi-Transparent Perovskite Solar Cells with a Cross-Linked Hole Transport Layer

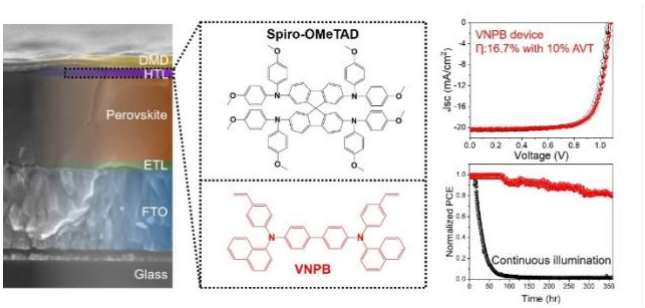

Vitae

Jae Choul Yu received his Ph. D (February 2018) in Materials Science and Engineering from Ulsan National Institute of Science and Technology (UNIST) and was a post doctoral researcher in Prof. Myoung Hoon Song's group in UNIST. He is currently a research fellow with the Department of Materials Science and Engineering at Monash University supervised under Prof. Jacek Jasieniak. His research focuses on perovskite optoelectronic devices such as solar cells, light-emitting diodes, semi-transparent and monolithic tandem devices.

Jingsong Sun received his B.S and M.E degrees in Applied Chemistry and Materials Science and Engineering, respectively, from Beijing University of Chemical Technology. He is currently a PhD student in the Department of Materials Science and Engineering, Monash University. His research interests focus on the efficient charge transporting materials and surface engineering in perovskite solar cells.

Naresh Chandrasekaran is a Research Fellow at Monash University and a Visiting S cientist at CSIRO, Australia. He received his PhD in Physics and Materials Engineeri ng from Monash University and Indian Institute of Technology Bombay in 2018. His r esearch interests include fabrication and charge carrier dynamics characterization in per ovskites and organic optoelectronic devices.

Christopher Dunn is a Research Scientist in the Nanomaterials and Devices Team in the Manufacturing Business Unit at CSIRO. Over the past 15 years, Chris has been working with electroactive materials for applications in photovoltaics, transistors (OFE T) and lighting (OLED). He is currently working on an ARENA project on the devel opment of semi-transparent perovskite solar cells that will be integrated as part of the manufacturing process to add extra value and functionality to commercial windows. Chris has a long-standing interest in the self-organising properties of materials and the consequences this has for their structure, properties and functions.

Anthony Chesman is a Senior Research Scientist at the Commonwealth Scientific an d Industrial Research Organisation (CSIRO) and the Team Leader of the Nanomaterial s and Devices Team. After completing his PhD in 2011 at Monash University on the magnetic properties of high nuclearity 3d/4f metal complexes, Dr Chesman moved int o the field of renewable energy at CSIRO, with a particular focus on solar cells com prising non-toxic and earth abundant materials. His current interests include nanocrysta l synthesis, solution-processed solar cell fabrication, and photocatalysis.

Jacek Jasieniak completed a Bachelor of Science (First Class Honours) from Flinders University (2003) and a Ph.D. from the University of Melbourne (2008). He then un dertook postdoctoral work at the Commonwealth Scientific and Industrial Research Or ganisation (CSIRO) and was a Fulbright Scholar at the University of California Santa Barbara (2011 to 2012). In 2012, he returned to CSIRO, progressing to a senior resea rch scientist and then group leader. In 2015, he moved to Monash University, where h

e is the current Director of the cross-disciplinary Monash Energy Institute and Profess or in the Materials Science & Engineering Department. Jacek's research interests inclu de the development of nanomaterials and their use in various next-generation energy t echnologies.